

## A new photolysis laser-induced fluorescence instrument for the detection of H<sub>2</sub>O and HDO in the lower stratosphere

J. M. St. Clair,<sup>a)</sup> T. F. Hanisco, E. M. Weinstock, E. J. Moyer,<sup>b)</sup> D. S. Sayres, F. N. Keutsch,<sup>c)</sup> J. H. Kroll,<sup>d)</sup> J. N. Demusz, N. T. Allen, J. B. Smith, J. R. Spackman,<sup>e)</sup> and J. G. Anderson

Department of Chemistry and Chemical Biology, Harvard University, Cambridge, Massachusetts 02138, USA

(Received 7 September 2007; accepted 18 May 2008; published online 16 June 2008)

We present a new instrument, Hoxotope, for the *in situ* measurement of H<sub>2</sub>O and its heavy deuterium isotopologue (HDO) in the upper troposphere and lower stratosphere aboard the NASA WB-57. Sensitive measurements of  $\delta D$  are accomplished through the vacuum UV photolysis of water followed by laser-induced fluorescence detection of the resultant OH and OD photofragments. The photolysis laser-induced fluorescence technique can obtain S/N > 20 for 1 ppbv HDO and S/N > 30 for 5 ppmv H<sub>2</sub>O for 10 s data, providing the sensitivity required for  $\delta D$  measurements in the tropopause region. The technique responds rapidly to changing water concentrations due to its inherently small sampling volume, augmented by steps taken to minimize water uptake on instrument plumbing. Data from the summer 2005 Aura Validation Experiment Water Isotope Intercomparison Flights (AVE-WIIF) out of Houston, TX show agreement for H<sub>2</sub>O between Hoxotope and the Harvard water vapor instrument and for HDO between Hoxotope and the Harvard ICOS water isotope instrument, to within stated instrument uncertainties. The successful intercomparison validates Hoxotope as a credible source of  $\delta D$  data in the upper troposphere and lower stratosphere. © 2008 American Institute of Physics. [DOI: 10.1063/1.2940221]

### INTRODUCTION

Water vapor in the upper troposphere and lower stratosphere (UT/LS) plays a critical role in the climate system of the earth through the absorption of infrared radiation and through the formation of cloud and aerosol particles.<sup>1</sup> Water vapor also plays a key role in coupling chemistry and climate in the stratosphere.<sup>2</sup> Reliable long-term climate forecasts require precise and accurate descriptions of the interaction between UT/LS water content and changes in global climate.<sup>3–5</sup> For the stratosphere, the exact nature of this interaction depends on the mechanism that controls the transport of water across the tropopause.<sup>6</sup>

Possible mechanisms range from slow, large-scale diabatic ascent to rapid, localized injection via convection (e.g., Holton and Gettelman<sup>7</sup> and Dessler and Sherwood<sup>8</sup>). These two mechanisms for controlling stratospheric water vapor may differ in their sensitivity to climate change: if the water vapor concentration entering the LS ( $[H_2O]_{LS}$ ) is influenced by convection, then warming the surface of the earth and ocean systems, with a subsequent increase in strong convection, could in turn increase  $[H_2O]_{LS}$  as has been observed

for the UT.<sup>9</sup> If the stratospheric entry humidity is regulated by the minimum tropopause temperature, then the concomitant cooling of the tropical tropopause may decrease  $[H_2O]_{LS}$ .

Observations of water isotopic abundance can provide insight and quantitative constraints to the mechanisms that determine stratospheric humidity.<sup>10,11</sup> The heavy deuterium isotopologue (HDO) preferentially condenses from the gas phase, resulting in dramatic reductions in the ratio of  $[HDO]/[H_2O]$  as air ascends from the boundary layer to the tropopause. The degree of isotopic separation is typically stated in terms of  $\delta D$ , where

$$\delta D = \left( \frac{([HDO]/[H_2O])_{\text{sample}}}{([HDO]/[H_2O])_{\text{V-SMOW}}} - 1 \right) 1000, \quad (1)$$

and V-SMOW refers to Vienna standard mean ocean water, with a  $[HDO]/[H_2O]$  ratio of  $3.115 \times 10^{-4}$ .<sup>12</sup> Slow ascent is often described by a simple thermodynamic model called Rayleigh distillation, which predicts a stratospheric  $\delta D = -900\%$ .<sup>13</sup> A stratosphere strongly influenced by convective transport would be less depleted in HDO due to the lofting of HDO-rich ice formed at lower altitudes.

In the lower troposphere, the  $\delta D$  profile largely follows the Rayleigh profile.<sup>14</sup> Water isotope measurements in the stratosphere (e.g., Moyer *et al.*,<sup>10</sup> Johnson *et al.*,<sup>15</sup> and McCarthy *et al.*<sup>16</sup>) and tropical UT (e.g., Kuang *et al.*<sup>17</sup>) obtained a  $\delta D \sim -650\%$  for water vapor entering the stratosphere, representing a convective signature on UT/LS water vapor. More recent *in situ* measurements indicate that ice from convective detrainment does in fact enrich the UT and subsequently the LS.<sup>18</sup> Models are able to reproduce obser-

<sup>a)</sup>Present address: Geology and Planetary Sciences Division, California Institute of Technology, Pasadena, CA 91125. Electronic mail: jstclair@huarp.harvard.edu.

<sup>b)</sup>Present address: Department of Geophysical Science, University of Chicago, Chicago, IL 60637.

<sup>c)</sup>Present address: Department of Chemistry, University of Wisconsin, Madison, WI 53706.

<sup>d)</sup>Present address: Aerodyne Research, Inc., Billerica, MA 01821.

<sup>e)</sup>Present address: Chemical Sciences Division, NOAA Earth System Research Laboratory, Boulder, CO 80305.

vations in the stratosphere with a mechanism that combines convective<sup>19,20</sup> and/or gradual dehydration with moistening via ice evaporation.<sup>21</sup> A common feature of these mechanisms is that convection moistens and isotopically enriches air in the UT that subsequently enters the stratosphere with depletions of  $\delta D \sim -650\%$ . An intriguing alternative is that moist air is transported directly to the overworld stratosphere via convection.<sup>8</sup> Recent *in situ* and remote measurements establish the existence of the direct injection route for overworld water vapor, although the relative importance of direct injection is still unclear.<sup>22–24</sup> *In situ* measurements of water vapor and lofted ice isotope ratios promise to clarify the relative importance of the transport mechanisms.

The recent result of Hanisco *et al.*<sup>24</sup> was made possible by the development of a new *in situ* water isotope instrument capable of the accuracy and precision required for water isotopes to serve as a tracer of convection and stratosphere-troposphere exchange. That instrument, named Hoxotope because of its development lineage from a high altitude, aircraft-based *in situ* HO<sub>x</sub> instrument,<sup>25</sup> has flown aboard the NASA WB-57 during an engineering test flight series in January 2005 and the Aura Validation Experiment Water Isotope Intercomparison Flights (AVE-WIIF) in summer 2005. In this paper, we describe the development of a new photolysis laser-induced fluorescence (LIF) technique for measuring the water isotopologues H<sub>2</sub>O and HDO and the benefits of the technique, such as a rapid instrumental response to changing water concentrations. Laboratory calibration is vital to Hoxotope operation, and so calibration technique and data are discussed in detail. Instrument intercomparisons for the measurements of both H<sub>2</sub>O and HDO are made using data from AVE-WIIF, validating the  $\delta D$  measured by Hoxotope and demonstrating that the photolysis-LIF technique is a successful method for measuring UT/LS H<sub>2</sub>O and HDO. The technique also possesses the attributes necessary for a future accurate, contamination-free measurement of lofted ice isotope ratios.

## MEASUREMENT TECHNIQUE

The isotopes of water (H<sub>2</sub>O and HDO) are detected with a combination of photolysis and LIF. The Hoxotope instrument uses a new photolysis system to produce OH and OD from H<sub>2</sub>O and HDO. The OH and OD radicals are subsequently detected with the same technique and much of the same equipment used to detect OH with the Harvard ER-2 HO<sub>x</sub> instrument.<sup>25</sup> Like the ER-2 HO<sub>x</sub> instrument, the Hoxotope instrument uses a ducted flow system to direct OH and OD radicals into an LIF detection region. The new photolysis system is positioned upstream of the LIF detection region. Thus, the detection of H<sub>2</sub>O and HDO involves two independent steps, each occurring in separate volume elements. This approach differs from the Lyman- $\alpha$  photofragment fluorescence technique that detects the fluorescence from excited state OH produced directly from the photolysis of H<sub>2</sub>O.<sup>26</sup> The Lyman- $\alpha$  photofragment fluorescence technique does not provide a measurement of HDO.

The photolysis-LIF technique uses vacuum ultraviolet (VUV) light to produce ground state OH and OD

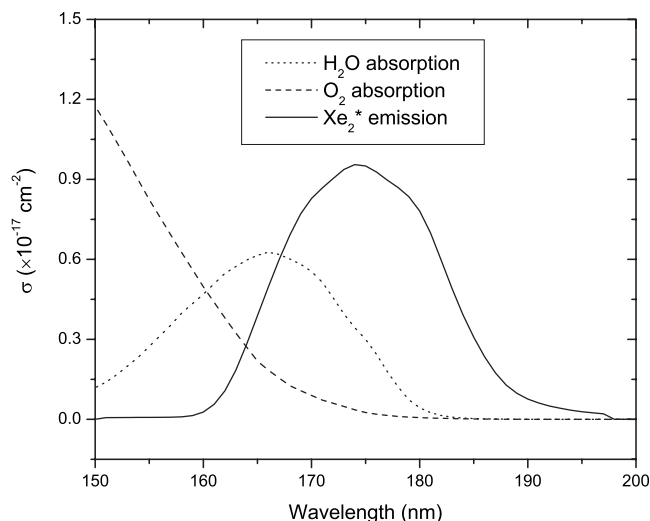
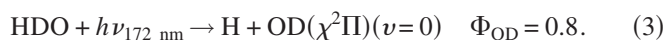
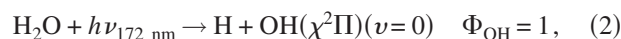
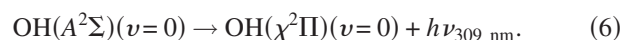
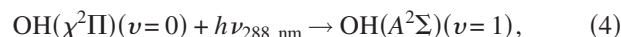


FIG. 1. The measured output of the 172 nm Xe excimer lamp emission is shown along with the absorption spectra of water and oxygen. (Refs. 30–32) Absorption by water results in photolysis, allowing for detection by LIF.



The quantum yield of OH in Eq. (2) is 1.<sup>27</sup> The yield of OD in Eq. (3) is approximately 0.8, although this yield is wavelength dependent.<sup>28,29</sup> The photolysis step is performed by the output of a xenon excimer (Xe<sub>2</sub><sup>\*</sup>) lamp that is centered at 172 nm. The emission of this lamp overlaps well with the continuum absorption feature of water centered at 165 nm, shown in Fig. 1. The absorption cross section of HDO is similar to that of H<sub>2</sub>O, but has a slightly different temperature dependence.<sup>30,31</sup> The competing absorption by O<sub>2</sub> requires photolysis at low pressures.<sup>32</sup>

OH and OD are detected further downstream via LIF using rotational state selective excitation at wavelengths near 288 nm. The relative abundance of HDO and H<sub>2</sub>O requires that the detection scheme be several orders of magnitude more sensitive to OD than to OH. The OH transition used in this detection scheme is part of a weak satellite branch of the  $\chi^2\Pi$  OH ( $v=0$ )  $\rightarrow$   $A^2\Sigma^+$  ( $v=1$ ) band originating near 282 nm.<sup>33</sup> The  ${}^{\text{O}}P_{12}(7.5)$  rotational transition is chosen because it lies near the strongest  $\chi^2\Pi$  OD ( $v=0$ )  $\rightarrow$   $A^2\Sigma^+$  ( $v=1$ ) rotational transition, the  $Q_1(3.5)$  line.<sup>34,35</sup> The OH transition is weak because of unfavorable electronic transition selection rules rather than a low ground state rotational population. Consequently, the measurement does not have the strong temperature dependence typical of infrared spectroscopic detection. Both OH and OD fluoresce via the same mechanism that begins with collisional relaxation of the excited vibrational state:<sup>36,37</sup>



OH and OD are thus excited with tunable light at 288 nm and the fluorescence is detected at 309 nm in a manner

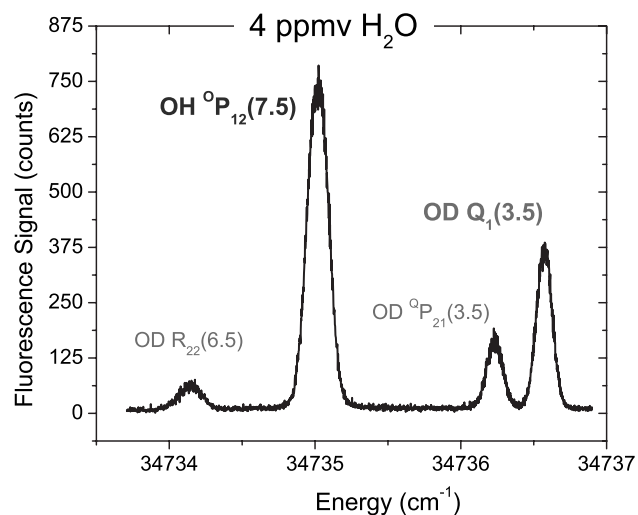


FIG. 2. The rotational spectrum of OH and OD around 287.9 nm, for 4 ppmv H<sub>2</sub>O and ~1.1 ppbv HDO. The OD lines are from the strong *P*, *Q*, and *R* bands of the  $A^2\Sigma^+ \leftarrow X^2\Pi(1,0)$  transition, and the OH line is from a weak satellite  ${}^0P$  branch of the  $A^2\Sigma^+ \leftarrow X^2\Pi(1,0)$  transition centered at 282 nm. The OH  ${}^0P_{12}(7.5)$  and OD  $Q_1(3.5)$  are used for H<sub>2</sub>O and HDO detection.

analogous to that used in the Harvard HO<sub>x</sub> instrument.<sup>25</sup> The OH and OD fluorescence signal from photolyzing 4 ppmv (parts per million by volume) of water is shown in Fig. 2.

## HARDWARE DESCRIPTION

### Sampling

The sampling section of the instrument provides particle separation, heating of the air sample, and pressure regulation with a design that also avoids measurement contamination. A rear-facing inlet made of stainless steel extends 23 cm normal to the side of the pallet and serves to exclude condensed phase material (Fig. 3, item A). The inlet is heated to prevent

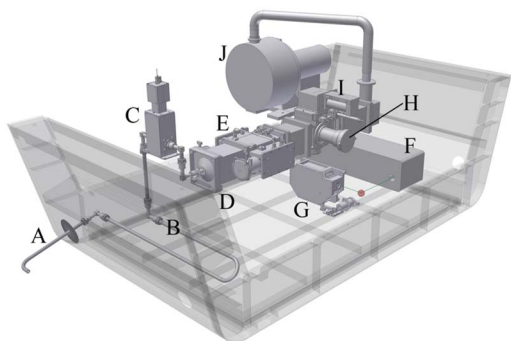


FIG. 3. (Color online) The instrument is shown in the WB-57 pallet, with most components removed to allow for better visualization of the central components of the instrument. Air is drawn into the instrument through a rear-facing inlet (item A) by a scroll pump (item J). The air is then heated as it travels through 1 m of stainless steel tubing (item B). The pressure of the instrument is maintained at 11.5 Torr by a pinch valve (item C). The flow is expanded and straightened (item D) before entering the photolysis cell (item E) where two Xe excimer lamps generate OH and OD from H<sub>2</sub>O and HDO. 288 nm light provided by the doubled output of a Nd<sup>3+</sup>:YAG (item F) pumped dye laser (item G) excites the hydroxyl radicals. OH and OD are detected with a 22 pass UV White cell (item H) and a gated PMT (item I) collects the fluorescence. Immediately following the detection axis is a duct containing temperature, pressure, and flow velocity measurements.

water uptake; four 10 W cartridge heaters in a copper housing are clamped around the inlet tubing immediately inside of the pallet and are controlled via a thermostat to around 50 °C. A thermally insulating spacer isolates the inlet from the pallet.

Air is drawn into the instrument by a Varian TriScroll 600 dry pump, which provides 8.3 l/s pumping speed without the inconvenience of oil and with virtually no modification needed for flight (Fig. 3, item J). The pump is mounted to the instrument via four vibration isolators (Barry Controls) so that pump vibration has no negative effect on instrument performance. A vent valve (BOC Edwards) is hardwired to the pump power and closes when the pump is powered up. Upon turning the pump off, the valve opens and air is drawn in through a box of desiccant (Drierite) to bring the instrument up to pressure with dry air.

While the detection scheme is largely invariant to temperature changes, the magnitude of the temperature correction is reduced by warming the airflow entering the instrument to near 25 °C before photolysis and detection. The heating is accomplished with 90 W of Minco heaters spread over 1 m of 1.25 cm OD electropolished stainless steel tubing (Fig. 3, item B) that follows the inlet. In addition to electropolishing the tubing, other steps were taken to minimize the residence time of water in the instrument: the interior of the tubing was coated with a hydrophobic fluoropolymer (Fluoropel, Cytonics) to minimize the uptake of water by the walls, and sections of tubing were joined using fittings that utilize L-shaped gaskets (*B* type VCO, Swagelok) to eliminate dead volume—regions in the flow system that are not continuously flushed and could retain water.

The tubing brings the airflow to a pinch valve (Swagelok, modified), which serves as an actively controlled conductance-limiting orifice, regulating the pressure in the photolysis and detection sections of the instrument (Fig. 3, item C). The valve operates by driving a plunger down onto a flexible tube. As the plunger pinches off the tube, the conductance of the tube is reduced and consequently the pressure in the instrument drops. The pinching action regulates airflow without adding stagnant “dead” volume, additional surface area, and the accompanying measurement time constant characteristic of a more traditional valve. The valve was modified to actively control the plunger with a stepper motor and a PID software algorithm. The instrument pressure is maintained at 11.5 Torr (1.53 kPa) by the pinch valve, independent of ambient pressure. The pressure-regulated air then flows through more electropolished stainless steel tubing and expands to a square 7.5 × 7.5 cm<sup>2</sup> duct, passing through a showerhead-style plate with nine evenly spaced 1.5 mm holes and a fine wire mesh (40 wires/cm) to straighten the flow before entering the photolysis cell (Fig. 3, item D).

### Photolysis cell

In traditional photolysis-LIF detection schemes, a laser provides the photolysis light with the advantage of generating a large amount of localized photofragments from the collimated beam. For our application, however, lamps provide sufficient photolysis with only a fraction of the size and weight of a laser. They also operate at much higher repetition

rates than excimer lasers, allowing our LIF system to operate at a high repetition rate and maintain its usual sensitivity.

Two Xe excimer lamps (XERADEX® 20, OSRAM Sylvania Inc.) provide 8 W each of nearly monochromatic 172 nm light for the photolysis of water. The lamps generate pulsed light at a repetition rate of 30 kHz, with 2  $\mu$ s long pulses. The lamp output is powerful and stable because excimer ( $\text{Xe}_2^*$ ) formation avoids self-absorption by Xe within the lamp. There is no cooling requirement for the lamps or their power supplies: they achieve 40% conversion efficiency from electrical power input to photon output.

The photolysis cell is shown in Fig. 3 (item E). The cylindrical lamps sit on either side of the cell, mounted closely to the duct to maximize the solid angle of the lamp output that enters the air flow. A three-sided retroreflector (Al mirrors with  $\text{MgF}_2$  coating from Esco Products Inc.) mounted behind each lamp also serves to enhance the 172 nm flux into the sample flow. The lamp housing is purged with dry nitrogen to prevent absorption by oxygen or water, and the pressure is kept at 15.2 psi (105 kPa) by a passive absolute pressure regulator (TAVCO Inc.). Lamp output is monitored using GaP photodiodes with sapphire windows capable of measuring light down to 150 nm, with one photodiode in each lamp housing (Roithner Lasertechnik).

Trace amounts of  $\text{H}_2\text{O}$  in the lamps produce excited state OH that fluoresces at 309 nm, which interferes with LIF signal. The geometry of the lamps was chosen to maximize photolysis yield and minimize background; rather than mounting the lamps parallel to the duct, a 5° angle was introduced with the down-flow end closer to the duct in an effort to decrease the amount of stray lamplight reaching the detection axes. Light from the lamps passes through 4.5 mm thick vacuum UV grade windows (Technical Glass Products) covering a  $13.3 \times 5.7 \text{ cm}^2$  opening in the duct. The windows are composed of Supracil/Corning 7980 and transmit down to 165 nm. O-rings seal between the windows and the duct. While thin windows are used to minimize loss of light to absorption in the window itself, the transmission of a given window turns out to be sufficiently variable from batch to batch that window quality matters more than window thickness. The transmission spectrum of each window was measured using a  $D_2$  lamp to evaluate window quality and ensure transmission down to 165 nm; the windows currently installed in the instrument transmit 50% at 167 nm. Although an increase in short wavelength transmission has a water photolysis benefit, the benefit to signal is tempered by an increased absorption from oxygen.

The lamps are powered with modified commercial 30 kHz, 5 kV power supplies (OSRAM Sylvania Inc.). A master timing circuit of our design controls the output of the supplies, synchronizing the output of the two lamps and the trigger of the detection laser, and thereby mostly eliminating 309 nm lamp scatter from the gated detection of the LIF signal. Figure 4 shows the timing scheme for the photolysis lamp and LIF laser pulses. The decrease in background from the synchronization is substantial, and is only possible because the lamps are pulsed rather than continuous. The circuit receives an enable command from the OSRAM board, as well as 15 V power, and returns to the board a 30 kHz,

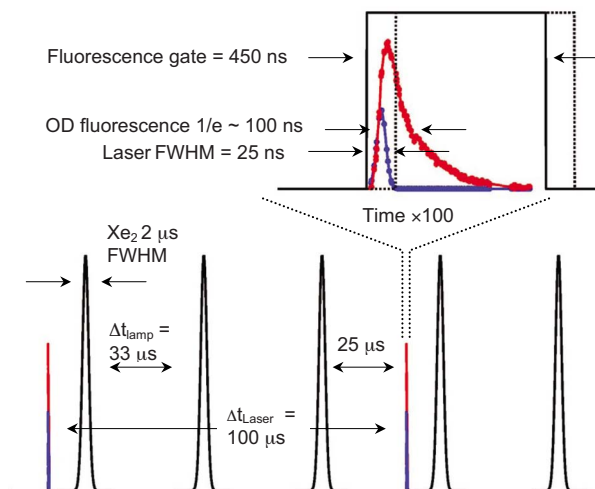


FIG. 4. (Color online) The timing scheme is shown for the synchronized 30 kHz photolysis and 10 kHz LIF detection. The time scale for the LIF excitation and fluorescence is expanded in the inset. The first PMT gate collects the entire fluorescence along with laser scatter (inset, solid) with the second gate collecting the long-lived fluorescence after the laser scatter (inset, dotted).

15 V pulse train. Optocouplers provide isolation between the two circuits on both the enable and the 30 kHz trigger sides. 5 V power and software-controlled enable commands for each lamp are delivered to the circuit. A variable output trigger, set by switches on the circuit, provides a 10 kHz trigger to the detection laser. The high voltages present on the lamp power supplies necessitated their enclosure in a pressure vessel to prevent corona discharge at low pressure. High voltage cables rated for use at low pressure (Reynolds Industries) attach to feedthroughs on the pressure vessel and connect to the lamps.

### Laser system

The laser system on the instrument has been upgraded since  $\text{HO}_x$  was last described in the literature.<sup>25</sup> The two  $\text{Nd}^{3+}$ :YLF pump lasers were replaced by one  $\text{Nd}^{3+}$ :YAG laser (Spectra Physics T40-X30, Mountain View, CA), providing 2.5 W at 532 nm, with a pulse width of 25 ns Q-switched at 10 kHz (Fig. 3, item F). The  $\text{Nd}^{3+}$ :YAG crystal is pumped by two 40 W laser diodes at 808 nm. Cooling of the laser is accomplished in two stages: thermoelectric coolers are used to control the temperature of the diodes while the laser dye, itself cooled by a different thermoelectric cooler, is circulated through the laser head to provide cooling there. The new laser, because of its tenfold increase in 532 nm power over the  $\text{Nd}^{3+}$ :YLF lasers, is able to pump the same dye laser but with considerable weight and space savings, as well as a significant simplification of the pump laser optical arrangement.

The dye laser (Fig. 3, item G; modified Chromatix, Mountain View, CA, no longer in operation) is longitudinally pumped, with wavelength selection accomplished using three prisms combined with a motor-actuated bellows for pressure tuning, and the linewidth further narrowed by an intracavity etalon. An intracavity barium borate crystal (Cleveland Crystals) doubles the laser output frequency to the UV. The more

powerful pump laser allows the use of a lower gain dye, Rhodamine 6G, reducing the likelihood of dye cell burns. A new method of tuning the dye laser was necessary for Hoxotope because simultaneously measuring OH and OD requires significantly greater wavelength stability. The new drive for tuning the etalon consists of a linear actuated stepper drive (Melles Griot). The drive is coupled into the pressure-sealed laser housing by a vacuum-tight ferrofluidic feedthrough (Ferrotec). The combination of the high precision linear stepper drive and the ferrofluidic coupler provide precise tuning over the OH and OD lines. The etalon tuning drive has an rms error less than  $0.01 \text{ cm}^{-1}$  over the  $3 \text{ cm}^{-1}$  wide scan shown in Fig. 2.

### Frequency reference cell

Like the ER-2  $\text{HO}_x$  instrument, Hoxotope utilizes a frequency reference cell to maintain control over the laser wavelength. The Hoxotope OD reference cell is identical to the  $\text{HO}_x$  instrument OH cell, with pure  $\text{D}_2\text{O}$  replacing  $\text{H}_2\text{O}$  to produce sufficient OD signal from the cell.<sup>25</sup> A few percent of the dye laser output is directed to the OD cell via an optical fiber. The cell is composed of a low-pressure quartz cell housing a glowing NiChrome filament and a  $\text{D}_2\text{O}$  source (heated  $\text{CaCO}_3 \cdot \text{D}_2\text{O}$ ), under 4 Torr (500 Pa) of  $\text{N}_2$  and 1 Torr (100 Pa) of  $\text{O}_2$ . OD radicals are produced on the filament and their LIF is detected at 309 nm with a filtered-photomultiplier tube (PMT) system. The OH line position is not measured directly; the etalon drive mechanism is precise enough ( $\pm 0.01 \text{ cm}^{-1}$ ) to ensure that the OH line position is easily obtained by moving a fixed number of steps from the OD line position.

### Detection axes

A white cell with mirrors on either side of the tube, 260 mm apart, provides 22 passes of the excitation laser (Fig. 3, item H). Only the center  $2 \times 2 \text{ cm}^2$  of the flow is imaged for detection by the PMTs (Fig. 3, item I). An interference filter (Barr Assoc., Westford, MA) optimized for simultaneous detection of OH and OD is used: it is centered at 309 nm and has a 6 nm (full width at half maximum) bandwidth, with an optical density of 8 at the laser lines and an optical density of  $>5$  from 200 to 700 nm (the PMT response range). The narrow filter cuts down our background considerably by greatly reducing the amount of Rayleigh and chamber scattering seen by our PMT—the background for recent flights was around  $6 \text{ counts s}^{-1}$  in the stratosphere. Background is also greatly reduced because Hoxotope is a pump-down system; the fluorescence lifetime is increased by the lower operational pressure and the PMT gating scheme can separate the prompt Raman and Rayleigh scattering from the longer lived OH and OD fluorescence. The inset in Fig. 4 shows the signal from laser scatter and long-lived OD fluorescence as a function of time, with the two PMT gates shown in black. The first PMT gate collects the entire fluorescence along with laser scatter (solid line) with the second gate collecting the long-lived fluorescence after the laser scatter (dotted line). The contribution of solar scatter to the

signal background is eliminated because Hoxotope is a closed system, further reducing the background.

## THE DETERMINATION OF OH AND OD CONCENTRATIONS

The concentrations of OH and OD at 288 nm are determined from the PMT signal using the same relations explained in detail for the detection of OH at 282 nm (Wennberg, 1994). One significant difference is that the OH and OD concentrations are not reported in this experiment, but are used as intermediate terms to determine  $\text{H}_2\text{O}$  and HDO concentrations. For this instrument it is important to determine the concentrations of OH and OD precisely, but absolute accuracy is not a requirement. Thus, calibrations for OH and OD sensitivities are not performed on a regular basis. The sensitivities are determined once, and corrections to these sensitivities are made for variations in temperature, pressure, and photon collection efficiency for individual calibration runs and aircraft flights. The OH and OD concentrations are related to the signal collected at the PMT by the following relationship:

$$[\text{OH}] = \text{signal} / (C_{\text{OH}} \times Q_{\text{OH}} \times N_{2 \text{ corr, OH}} \times T_{\text{corr, OH}}), \quad (7)$$

$$[\text{OD}] = \text{signal} / (C_{\text{OD}} \times Q_{\text{OD}} \times N_{2 \text{ corr, OD}} \times T_{\text{corr, OD}}). \quad (8)$$

In these relationships  $C$  is the sensitivity calibration constant,  $Q$  is the fluorescence efficiency,  $N_{2 \text{ corr}}$  is the  $\text{N}_2$  Raman correction for optical collection efficiency, and  $T_{\text{corr}}$  is the correction term for the rotational population temperature dependence.

The sensitivity calibration constant,  $C$ , was determined by adding a known amount of OH into the system using the reaction of H atoms with  $\text{NO}_2$



In this calibration a known amount of  $\text{NO}_2$  is added to excess H atoms, as described by Wennberg *et al.*<sup>25</sup> The constants used for Hoxotope are  $C_{\text{OH}} = 2.3 \times 10^{-6}$  and  $C_{\text{OD}} = 7.7 \times 10^{-3}$ . The sensitivity of the system to OH is three orders of magnitude smaller than OD because of the weaker linestrength of the OH transition.

The fluorescence efficiency,  $Q$ , is the fraction of OH or OD excited to the  $A^2\Sigma^+(v=1)$  that fluoresces from the  $A^2\Sigma^+(v=0)$  state [Eqs. (5) and (6)]. This term is the product of two fractions. The first is the fraction of radicals in the  $A^2\Sigma^+(v=1)$  that relax to  $A^2\Sigma^+(v=0)$ . The second is the fraction of radicals in  $A^2\Sigma^+(v=0)$  that fluoresce. The denominator in each term is the total relaxation rate from each excited vibrational state

$$Q = \frac{k^{\nu-\nu} [M]}{k_{\nu',\nu=1}^{\text{rad}} + k^{\nu-\nu} [M] + k_{\nu',\nu=1}^{\text{Q}} [M]} \times \frac{k_{\nu',\nu=0}^{\text{rad}}}{k_{\nu',\nu=0}^{\text{rad}} + k_{\nu',\nu=0}^{\text{Q}} [M]}. \quad (10)$$

The rate constants for vibrational relaxation ( $k^{\nu-\nu}$ ), electronic state quenching ( $k^{\text{Q}}$ ), and radiative emission ( $k^{\text{rad}}$ ) of the  $A^2\Sigma^+$  state of OH and OD are shown in Table I. The fluorescence efficiency is temperature and pressure dependent. Typical values and the standard deviation for  $Q$  in the

TABLE I. Quenching rate constants (units of  $\text{cm}^3 \text{molecule}^{-1} \text{s}^{-1}$ ) and radiative decay rates (units of  $\text{s}^{-1}$ ) for  $A^2\Sigma^+ \text{OH}$  and  $A^2\Sigma^+ \text{OD}$  (Refs. 36, 37, and 40–47).

	OH ( $\nu'=0$ )	OH ( $\nu'=1$ )	OD ( $\nu'=0$ )	OD ( $\nu'=1$ )
$k^{v-v} \text{N}_2$	...	$2.2 \times 10^{-10}$	...	$8.6 \times 10^{-11}$
$k^{v-v} \text{O}_2$	...	$2.5 \times 10^{-11}$	...	$3.7 \times 10^{-11}$
$k^Q \text{N}_2$	$1.55e^{(140/T)} \times 10^{-11}$	$2.8 \times 10^{-11}$	$3.0 \times 10^{-11}$	$5.5 \times 10^{-11}$
$k^Q \text{O}_2$	$1.06 \times 10^{-10}$	$1.8 \times 10^{-10}$	$1.13 \times 10^{-10}$	$1.2 \times 10^{-10}$
$k^{\text{rad}}$	$1.44 \times 10^6$	$1.32 \times 10^6$	$1.44 \times 10^6$	$1.32 \times 10^6$

Hoxotope instrument, during a laboratory calibration or a flight, are  $Q_{\text{OH}}=0.114 \pm 0.005$  and  $Q_{\text{OD}}=0.043 \pm 0.003$ .

The correction for optical collection efficiency,  $N_{2 \text{ corr}}$ , is based on the sensitivity of the detection system to the first Stokes transition of the  $\text{N}_2$  Raman scattering of the 288 nm laser light. This band is centered at 309 nm, at the middle of the OH and OD fluorescence bands. Thus, the sensitivity of the detection system to photons from  $\text{N}_2$  Raman scattering is directly proportional to that of the OH and OD fluorescence. It is useful to use the  $\text{N}_2$  Raman sensitivity as a reference because the abundance of  $\text{N}_2$  is easily determined in both the laboratory and in flight. The sensitivity of the detection system to  $\text{N}_2$  Raman,  $S(\text{N}_{2,\text{ref}})$ , was determined the laboratory at the same time that the OH and OD sensitivity constants  $C_{\text{OH}}$  and  $C_{\text{OD}}$  were determined. The reference value for  $\text{N}_2$  Raman is  $S(\text{N}_{2,\text{ref}})=4.0 \times 10^{-15} \text{ counts molecule}^{-1} \text{ s}^{-1}$ . Typical values of  $S(\text{N}_{2,\text{ref}})$  in the laboratory and in flight are  $(3.6\text{--}4.4) \times 10^{-15} \text{ counts molecule}^{-1} \text{ s}^{-1}$ . The range in  $S(\text{N}_{2,\text{ref}})$  is due to small alignment changes in the LIF White cell that are caused by mechanical deformations in the laser bench. The correction term is the ratio of the measured value to the reference value,  $N_{2 \text{ corr}}=S(\text{N}_{2,\text{ref}})/S(\text{N}_2)$ . The correction term and its standard deviation, during a laboratory calibration or a flight, are typically  $N_{2 \text{ corr}}=1.0 \pm 0.1$ .

The temperature correction term,  $T_{\text{corr}}$ , is needed to account for changes in the ground rotational state populations of OH and OD. The correction term is the relative population of the ground state at the time of measurement compared to the reference according to the equation

$$T_{\text{corr}} = e^{E/k_B[1/(T_{\text{ref}}-1/T)]}, \quad (11)$$

where  $T_{\text{ref}}=303 \text{ K}$  is the calibration temperature and  $k_B=0.695 \text{ 04 cm}^{-1}/\text{K}$ . The ground state of the OH  $^{\text{O}}P_{12}(7.5)$  transition is  $E=1079 \text{ cm}^{-1}$ . The ground state energy of the OD  $Q_1(3.5)$  transition is  $E=214.7 \text{ cm}^{-1}$ . Calibration runs in the laboratory have shown that the precision of the measurement is improved by accounting for the temperature (Fig. 5). The correction to OH is  $\sim 1.7\% / ^\circ\text{C}$ , with a smaller correction for OD ( $0.3\% / ^\circ\text{C}$ ). Typical values and standard deviations are  $T_{\text{corr,OH}}=1.0 \pm 0.1$  and  $T_{\text{corr,OD}}=1.00 \pm 0.02$ .

## CALIBRATION

### Water source

The Hoxotope instrument is calibrated by adding air with a known amount of water into the sample tube. The carrier flow is composed of zero air (Airgas) further dried on a column of molecular sieve to reduce  $[\text{H}_2\text{O}]$  to below

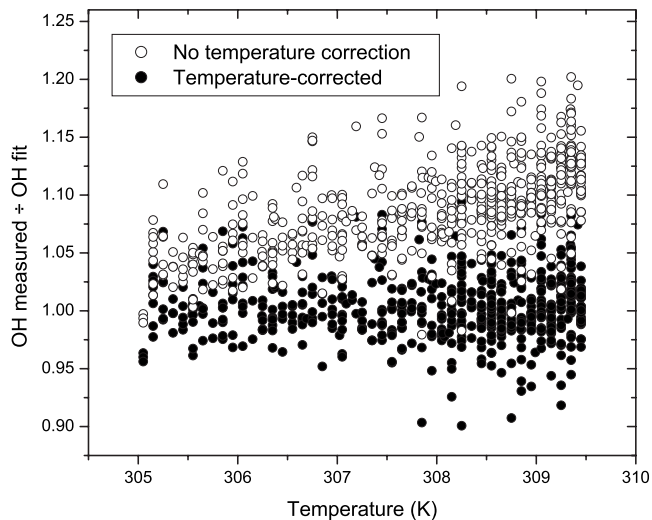


FIG. 5. Normalizing the OH signal by the fit value reveals a temperature trend in the data. A temperature correction of  $1.7\% / ^\circ\text{C}$  for OH and ( $0.3\% / ^\circ\text{C}$ ) for OD (not shown) is used to correct for the trend.

3 ppmv. A 20 slm (standard liters per minute) flow controller (MKS Instruments) sets the flow to achieve a pressure of 11.5 Torr (1.53 kPa) in the instrument. Water vapor is introduced into the flow using a single-stage bubbler, and its mixing ratio in the main flow ( $0\text{--}200 \text{ ppmv}$ ) is varied by a 50 sccm (standard cubic centimeter per minutes) flow controller. The bubbler creates a saturated headspace by releasing dry air into liquid water through a glass frit (Fig. 6, left panel). The saturated air flows from the bubbler to the flow controller and into the main air flow where it mixes before entering the instrument. Because the water saturation mixing ratio depends on the temperature and pressure of the bubbler, the bubbler temperature is continually measured and the pressure is kept very near to 1 atm (100 kPa).

Isotopic fractionation is inevitable for any water vapor generation method that relies on vapor pressure, including the bubbler system used for the routine calibration of Hoxotope. The performance of the bubbler, in particular its propensity to fractionate isotopes, has been investigated through the use of a droplet microinjector. The microinjector (Microdrop, part MD-K-130-010, Norderstedt, Germany) avoids fractionation by introducing water droplets directly into the flow where they completely evaporate without saturating the air (Fig. 6, right panel). Water is drawn from a small reser-

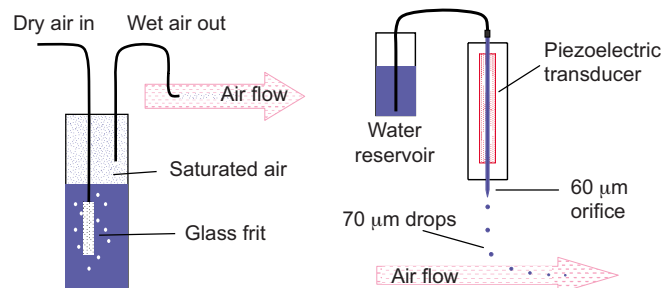


FIG. 6. (Color online) Two techniques for introducing water vapor into the instrument for laboratory calibration: saturated water addition (left panel) and water microdroplet injection (right panel). The two techniques differ in their propensity to fractionate water isotopes.

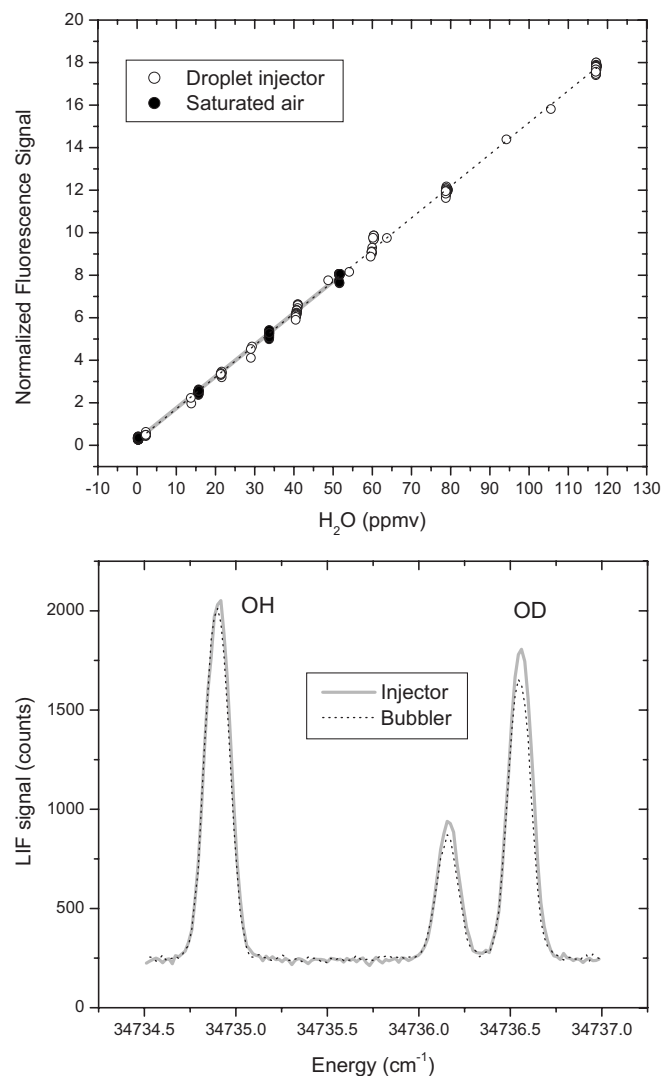


FIG. 7. Top panel: the normalized Lyman- $\alpha$  fluorescence signal resulting from both droplet injector and saturated air water addition techniques. Bottom panel: scans of the LIF signal (normalized to OH signal) using the two water addition methods makes apparent the isotopic fractionation introduced by the bubbler.

voir to a piezoelectric transducer that squeezes small droplets out of a 60  $\mu\text{m}$  orifice, generating 70  $\mu\text{m}$  diameter droplets (200 pl in volume). The amount of water vapor added to the flow is determined by the fixed droplet size and the adjustable frequency of the piezoelectric. The injector is calibrated by collecting the dispensed liquid over the period of an hour and then weighing the sample to determine the droplet water mass.

The two methods of generating water vapor produced nearly identical results as measured by the Lyman- $\alpha$  photofragment fluorescence instrument: signal from the two methods coincide and exhibit a linear response with increasing water mixing ratio (Fig. 7, upper panel).<sup>38</sup> The difference between the two methods appears when viewing the isotopic composition of their respective water vapor via LIF with Hoxotope: the microinjector water vapor contains about 7% more deuterated water than the bubbler water vapor (Fig. 7, lower panel). Background counts are high in this spectrum because it was generated early in the instrument develop-

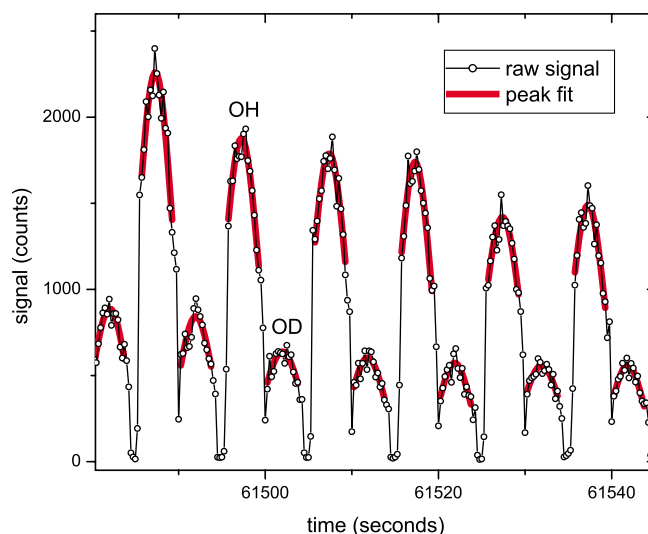


FIG. 8. (Color online) Effective OH and OD signals are extracted from the raw LIF data (line and circles) by fitting each transition to a Gaussian function (thick line). The Gaussian is used to determine H<sub>2</sub>O and HDO concentrations.

ment. During a calibration with the bubbler, the exact fractionation imposed by the vapor pressure isotope effect (VPIE) is determined using an expression for the temperature dependence of the VPIE (Ref. 19)

$$\ln(R_c/R_v) = -0.1 + 15\,013/T^2, \quad (12)$$

where  $R_c$  is the isotopic ratio of the condensate,  $R_v$  is the isotopic ratio of the vapor, and  $T$  is the temperature in Kelvin. The calibration water itself contains a  $\delta D$  of  $-(50.7 \pm 1.8)\text{‰}$  referenced to V-SMOW, determined by the average of samples sent to three different stable isotope laboratories (Boston University, University of Idaho, and University of Colorado) for analysis by mass spectrometry.

## Data analysis

The OH and OD fragments from the photolysis of water are detected by LIF, with the laser scanning alternately over the OH and OD lines, as shown in Fig. 8. Each scan takes 4 s per line, 10 s total. The thin line and circles are the raw signal from a flight on 3 July 2005. Effective OH and OD signals are extracted from the raw data by fitting each line to a Gaussian function, using a nonlinear least squares fit. The signal is then corrected for the vibrational relaxation, electronic quenching, and radiative lifetime of the excited state as discussed in the previous section on determining OH and OD concentrations. Backgrounds for the two transitions are determined from the fluorescence signal at an offline position measured after each OD scan. The offline position alternates between a position near the OD transition and the OH transition.

The VUV excimer lamp light initiates a considerable amount of photochemistry. O<sub>2</sub> absorbs strongly at 172 nm and reduces the photolysis yield of OH and OD (Fig. 1). This absorption also initiates the formation of ozone that leads to the removal of hydroxyl radical via reactions (16) and (18). The most important reactions are



Reactions that consume hydroxyl radicals reduce the instrument sensitivity to water vapor. Those reactions that are second order in  $[\text{HO}_x]$ , such as  $\text{OH} + \text{HO}_2$ , cause the calibration curve to become nonlinear at high  $[\text{HO}_x]$ , with instrument sensitivity to water vapor decreasing with increasing water vapor mixing ratio. It is possible, though cumbersome, to include a full chemical model when fitting the calibration curve. The nonlinear shape of the calibration curve is dominated by the reaction of OH and OD with  $\text{HO}_2$ , and so the loss of OH and OD can be adequately represented with just that reaction. The calibration curve can be fit using a simple equation that results from the analytic solution to the simplified chemistry model

$$[\text{OH}]_t = \frac{[\text{OH}]_0}{(kt[\text{OH}]_0 + 1)}, \quad (19)$$

where  $[\text{OH}]_0$ , the initial [OH], is  $[\text{OH}]_0 = \phi[\text{H}_2\text{O}]$ , with  $\phi$  being the effective photolysis yield, and  $[\text{H}_2\text{O}]$  being the water number density;  $k$  is the pressure and temperature-dependent reaction rate of the  $\text{OH} + \text{HO}_2$  reaction and  $t$  is the time between photolysis and detection. The kinetic loss term uses  $[\text{OH}]_0$  in place of the initial  $\text{HO}_2$  mixing ratio, a substitution made possible by Eqs. (2), (3), and (15).

The adjustable parameters in the least squares fit of the simplified model to the data are  $\phi$  and  $t$ . It is worth noting that  $\phi$  and  $t$  from this treatment absorb the effects of the chemistry not explicitly accounted for in the model (e.g., first-order OH loss), making them less physically connected. For example, reaction (16) is not included explicitly in Eq. (19), but it is effectively accounted for by a reduction in  $\phi$  and an increase in  $t$ . Data fits were conducted with both the full and the simplified models for a few calibration runs and the simplified model did an excellent job of describing the data. Figure 9 (top panel) shows a calibration run with the data fit using this approach.

$[\text{H}_2\text{O}]$  and  $[\text{HDO}]$  are determined by inverting Eq. (19) to obtain

$$[\text{H}_2\text{O}] = \frac{[\text{OH}]_t}{\phi(1 - kt[\text{OH}]_t)}, \quad (20)$$

$$[\text{HDO}] = \frac{[\text{OD}]_t}{\phi(1 - kt[\text{OH}]_t)}, \quad (21)$$

where  $\phi_{\text{H}_2\text{O}} = 5.94 \times 10^{-4}$ ,  $\phi_{\text{HDO}} = 5.90 \times 10^{-4}$ , and  $k = (4.8 \times 10^{-11} e^{250/T})$  for the  $\text{OH} + \text{HO}_2$  reaction.<sup>27</sup> The reaction rate for  $\text{OD} + \text{HO}_2$  is assumed to be similar and the same rate is used for determining HDO; any difference in  $k$  will be accounted for in the calibration curve. Figure 9

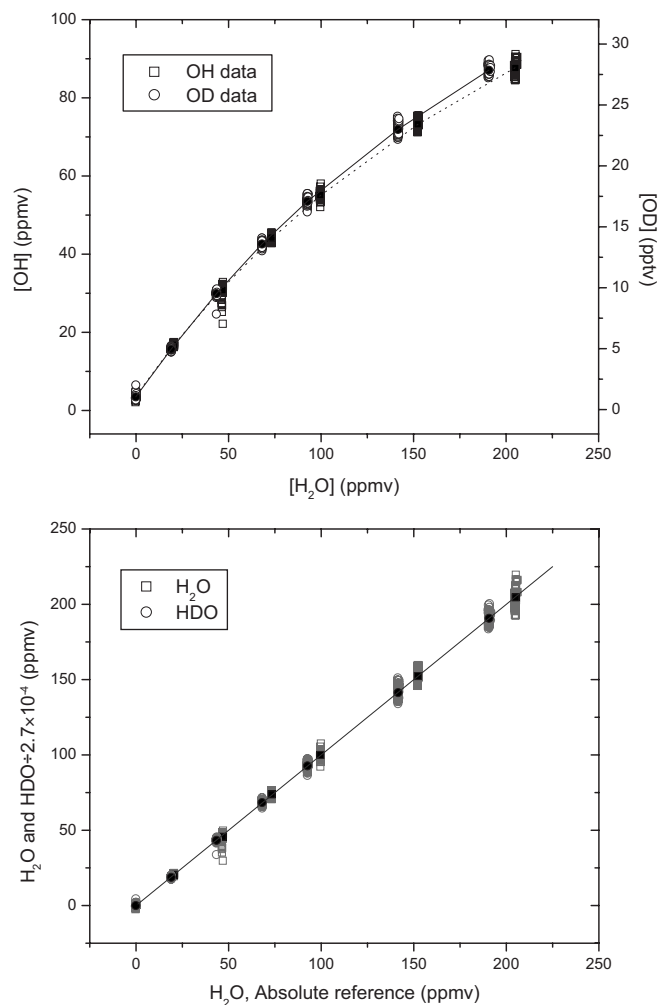


FIG. 9. Top panel: concentrations of  $\text{H}_2\text{O}$  and HDO from flight are determined using calibration curves obtained in laboratory. Mean laboratory data (solid symbols) are fit with a two-parameter expression, yielding the calibration curve (dashed for OH, solid for OD). OH and OD mixing ratios are uncalibrated. Bottom panel: water provided by the bubbler ( $x$  axis) is compared to the water calculated from the OH and OD signal, using the calibration curve ( $y$  axis). The solid symbols are mean values for each water concentration. The one-to-one line is provided as a metric to the data.

(bottom panel) shows the  $[\text{H}_2\text{O}]$  and  $[\text{HDO}]$  determined from the measured OH and OD plotted against the  $[\text{H}_2\text{O}]$  and  $[\text{HDO}]$  determined from the water addition system. The scaling factor for HDO accounts for the  $\delta D$  of the calibration water, the fractionation introduced by the bubbler, and the V-SMOW ratio. The resulting regression shows a strong agreement between the calculated water source and the water determined from the OH and OD signals. The regression is also notable for what it does not contain: it lacks any systematic biases or deviations from a linear relationship at high or low water, problems that would be detrimental to a  $\delta D$  measurement and that often plague absorption techniques. Once  $\text{H}_2\text{O}$  and HDO mixing ratios are determined using Eqs. (20) and (21), Eq. (1) is used to obtain  $\delta D$ .

#### Calibration uncertainty and in-flight accuracy

The uncertainty in the laboratory calibration is used to estimate the instrument measurement accuracy in flight. Uncertainties in the measurements of flow, pressure, tempera-

ture, and other measured and derived quantities contribute to the laboratory calibration uncertainty. Most of these uncertainties are small; for example, pressure and flow are typically measured with fractional uncertainties equal to or better than 1%. One of the largest uncertainties is associated with the concentration of the water vapor mixing ratio used in the calibration. The water vapor mixing ratio is determined from the vapor pressure of water in the bubbler, which is strongly dependent on temperature. The absolute uncertainty in the temperature measurement of the bubbler ( $\pm 0.5$  °C) corresponds to a fractional uncertainty in water vapor mixing ratio of  $\pm 3\%$ . That is, at 20 °C (293 K), the saturation mixing ratio of water and the corresponding  $1\sigma$  uncertainty used in the calibration is  $0.031 \pm 0.001$ . This and other known uncertainties are added in quadrature to determine an overall calibration uncertainty, and in-flight accuracy, of  $\pm 5\%$  for  $\text{H}_2\text{O}$  and HDO. Flight-to-flight variations in photolysis yield that might result from changes in lamp output or pumping speed, neither of which is explicitly corrected for in the data analysis, necessitate frequent calibrations.

The uncertainty of the ratio of  $[\text{HDO}]/[\text{H}_2\text{O}]$  in units of per mil is determined by propagating the fractional uncertainty of the ratio ( $\sigma_{\text{HDO}/\text{H}_2\text{O}}$ ) through Eq. (1), yielding the expression

$$\sigma_{\delta D} = \frac{[\text{HDO}]/[\text{H}_2\text{O}]}{([\text{HDO}]/[\text{H}_2\text{O}])_{\text{V-SMOW}}} 1000(\sigma_{\text{HDO}/\text{H}_2\text{O}}). \quad (22)$$

The uncertainty of the ratio  $[\text{HDO}]/[\text{H}_2\text{O}]$  is the square root of the sum of the squares of the HDO and  $\text{H}_2\text{O}$  measurement uncertainties,  $\sigma_{\text{HDO}/\text{H}_2\text{O}} = 0.07$ . For example, for  $\delta D = -500\text{‰}$ , the  $1\sigma$  uncertainty of the ratio  $[\text{HDO}]/[\text{H}_2\text{O}]$  expressed in units of per mil is  $\pm 35\text{‰}$ ; for  $\delta D = -750\text{‰}$  the uncertainty is  $\pm 18\text{‰}$ . Because of the nonintuitive behavior of  $\delta D$  uncertainties, we find it more useful to discuss accuracy and precision in terms of  $\text{H}_2\text{O}$  and HDO.

### In-flight calibration of detection sensitivity

In-flight variations in detection sensitivity are monitored by measuring the  $\text{N}_2$  Raman signal during the flight. The  $\text{N}_2$  Raman sensitivity is proportional to fluorescence detection sensitivity, allowing changes in fluorescence detection sensitivity to be tracked. The  $\text{N}_2$  Raman signal is measured continuously because the signal is at 309 nm, overlapping with the LIF detection wavelength. The sensitivity of the White cell to Raman scattering by  $\text{N}_2$  is measured at multiple times during a flight, as well as at least once during a calibration run. Any change in sensitivity is corrected for by adjusting the signal with the  $\text{N}_2$  Raman sensitivity, normalized to the value of a chosen laboratory calibration run. The correction is typically only a few percent. The  $\text{N}_2$  Raman calibrations at the end of a calibration run and at the end of a flight are conducted with the excimer lamp off to allow a measurement of the  $\text{N}_2$  Raman sensitivity at the OH and OD line positions. The  $\text{N}_2$  Raman calibrations during a flight only measure at the offline positions to avoid including LIF signal.

### Instrument operation considerations

When deciding on the optimal operating pressure and VUV flux, the nonlinear effects of the photochemistry were weighed against the increased signal from a high hydroxyl radical number density. Both a higher pressure and a greater VUV flux increase the amount of hydroxyl radical produced, but with diminishing returns to the instrument sensitivity for a given water vapor mixing ratio due to increased  $\text{O}_3$  production and subsequent increased first-order OH loss. Calibration data for pressures ranging from 7.5 Torr (1.0 kPa) to 19 Torr (2.5 kPa) were collected and the highest sensitivity was obtained at around 11.5 Torr (1.53 kPa). Similarly, the need for VUV from two lamps was considered by comparing calibration data with one lamp operating versus data with both lamps turned on. While the signal with two lamps is not twice that with one lamp ( $\sim 80\%$  increase for OD at 200 ppmv  $[\text{H}_2\text{O}]$  and 11.5 Torr [1.53 kPa]), the benefit increases with decreasing water vapor concentration and so provides an appreciated signal boost to the low-signal end of instrument operation. Flow velocity is another part of the photochemistry equation, with faster flow limiting loss of OH, but also limiting OH production by lowering  $\phi$ .

### INSTRUMENT PERFORMANCE

#### Sensitivity

In the laboratory, Hoxotope is capable of a signal to noise ratio of  $>20/1$  for 1 ppbv (parts per billion by volume) of HDO and a S/N of  $>30/1$  for 5 ppmv of  $\text{H}_2\text{O}$  in a 10 s measurement interval. The S/N of the ratio is determined primarily by the measurement of HDO which has the lower S/N. In the laboratory the S/N of the ratio HDO/ $\text{H}_2\text{O}$  is 17. At typical stratospheric values ( $[\text{HDO}] = 0.8$  ppbv,  $[\text{H}_2\text{O}] = 5$  ppmv, and  $\delta D = -500\text{‰}$ ) the precision in 10 s is  $\pm 0.04$  ppbv for HDO,  $\pm 0.02$  ppmv for  $\text{H}_2\text{O}$ , and  $\pm 30\text{‰}$  for  $\delta D$ . The 10 s measurement interval is determined from the mechanical limitations of the instrument. The scanning of the dye laser wavelength is accomplished mechanically by rotating an etalon and a finite amount of time is required to scan over each line and to drive the etalon to a new position. The total time of the measurement cycle is 10 s, with 4 s being spent scanning over each line. The instrument can be operated in another mode, detecting only HDO or  $\text{H}_2\text{O}$ . In this mode the data are nearly continuous at 4 Hz (the data acquisition rate) and would be limited by signal to noise and the instrument sampling time response.

#### Sampling time response

Abrupt changes in atmospheric water concentration and in isotopic depletion are fundamentally interesting structures that a scientifically useful water isotope instrument must be able to resolve, particularly if the instrument is configured to obtain a total water isotopes measurement. Water, with its propensity to adhere to surfaces, provides a considerable challenge to designing an instrument with a fast time response. The issues of water retention and instrument flush time have been minimized in Hoxotope through the use of a small sampling volume and large pump throughput, the avoidance of dead volume preceding detection, and the lib-

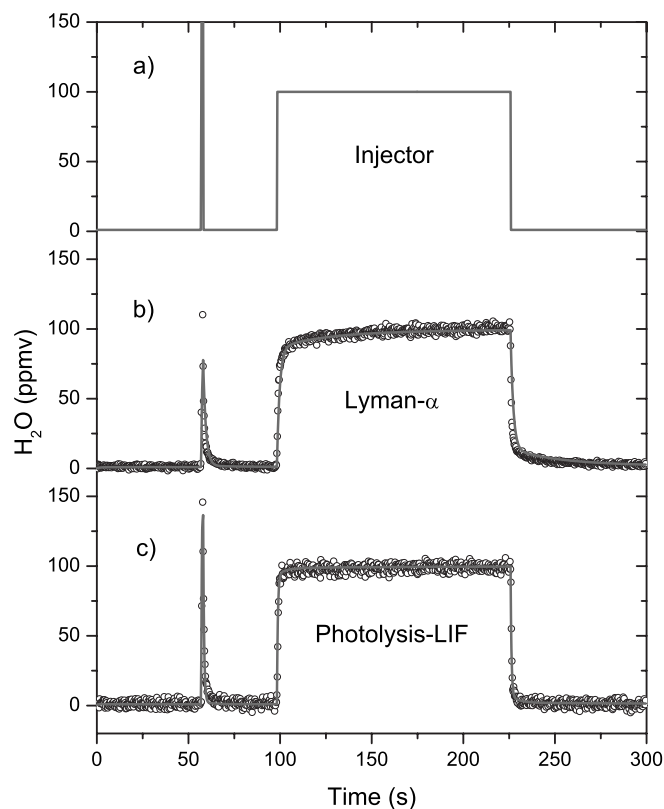


FIG. 10. The time response is shown for  $\text{H}_2\text{O}$  measured by a Lyman- $\alpha$  hygrometer and the concurrent measurement of photofragment OH by LIF. A microinjector was used to introduce a known amount of  $\text{H}_2\text{O}$  [panel (a)]. The symbols in panel (b) show the 4 Hz water measurement of the Lyman- $\alpha$  hygrometer, while panel (c) shows the 4 Hz photolysis-LIF signal. The solid lines are a multiexponential fit to the signal from the two techniques.

eral use of hydrophobic coatings. The small sampling volume is unique to the photolysis-LIF technique—any OH and OD that reaches the Hoxotope instrument walls is permanently removed, making uptake of water on the post-photolysis ducting irrelevant to the time constant of the instrument. The time resolution is currently limited by the time needed to make the LIF measurement.

The rapid time response of the photolysis-LIF method of water detection has been demonstrated in the laboratory by directly comparing it to the molecular detection of water by Lyman- $\alpha$  fluorescence.<sup>38</sup> The two techniques, OH radical detection and Lyman- $\alpha$  molecular water detection, were installed inline on the same flow system with a Lyman- $\alpha$  detection axis immediately after the LIF detection axis. Water was added using the microdroplet injector technique to allow a rapid time response from the water source.

The measurements of a 100 ppmv, 2 min. long water pulse by the two techniques are shown in Fig. 10. The photolysis-LIF response was modeled by

$$[\text{H}_2\text{O}]_{\text{measured,LIF}} = 100 \text{ ppmv} (0.98e^{-t/\tau_1} + 0.015e^{-t/\tau_2} + 0.005e^{-t/\tau_3}), \quad (23)$$

at some time  $t$  after the turnoff, where  $\tau$  represents the various time constants of the instrument: flush time ( $\tau_1=1$  s), adsorption onto walls ( $\tau_2=35$  s and  $\tau_3=100$  s), and absorption into O-rings ( $\tau_2$  and  $\tau_3$ ). The instrument subsequently observes a residual 1% (+1 ppmv) 10 s after the water pulse

and 0.3% (+0.3 ppmv) 60 s later. Molecular detection by Lyman- $\alpha$  experienced a longer time constant resulting from the exposure of the sample air to a greater amount of surface area prior to detection, represented by

$$[\text{H}_2\text{O}]_{\text{measured,Lyman-}\alpha} = 100 \text{ ppmv} (0.80e^{-t/\tau_1} + 0.15e^{-t/\tau_2} + 0.05e^{-t/\tau_3}), \quad (24)$$

with the additional surface area resulting in a greater contribution from the longer time constant terms. In the LIF case,  $\text{H}_2\text{O}$  is photolyzed to OH after exposure to just 200  $\text{cm}^2$  of surface area, whereas the Lyman- $\alpha$  measurement was made after exposure to nearly 3000  $\text{cm}^2$ . This example illustrates that the LIF-photolysis method is less sensitive to water uptake by instrument walls than is Lyman- $\alpha$  or other molecular water detection schemes for equivalent sampling conditions. In flight, the Harvard Lyman- $\alpha$  water vapor instrument experiences considerably higher flow rates than were used in this example.

## RECENT FLIGHT RESULTS

The summer 2005 Aura Validation Experiment Water Isotope Intercomparison Flights (AVE-WIIF) were conducted out of Ellington Field in Houston, Texas. The flight series was comprised of one test flight and three intercomparison flights aboard the NASA WB-57. Hoxotope was flown in the third pallet position of the WB-57. AVE-WIIF provided an excellent opportunity to compare the performance of Hoxotope to an established water vapor instrument (Harvard water vapor, hereafter HWV) (Ref. 38) and another HDO instrument with a different detection technique (Integrated Cavity Output Spectroscopy, ICOS).<sup>39</sup> Flying with the ram air-fed HWV provided an indirect metric for evaluating the accuracy of Hoxotope, and also allowed for the investigation of issues such as contamination and sampling time constants—performance attributes that go beyond accuracy and cannot be accessed via cross calibration in the laboratory. Intercomparison with ICOS, a cavity-enhanced mid-IR absorption spectrometer, is less definitive because both instruments are new to measuring HDO. The HDO intercomparison is still very valuable, because the low concentrations of HDO are a greater test of instrument performance and are more likely to reveal instrumental issues.

General agreement between Hoxotope (abbreviated as  $\text{HO}_x$ )  $\text{H}_2\text{O}$  and HWV  $\text{H}_2\text{O}$  over the three orders of magnitude range in  $[\text{H}_2\text{O}]$  is illustrated with a regression between the two instruments (Fig. 11). Due to the high-altitude emphasis of the AVE-WIIF flight profiles, the vast majority of data are below  $[\text{H}_2\text{O}]=75$  ppmv. Data included in the fit were restricted to  $[\text{H}_2\text{O}]\leq 200$  ppmv. The linear regression yielded a slope of 1.00, indicating a strong agreement ( $R^2=0.98$ ) between the calibrations of the two instruments. The scatter in the trend is the result of the decreased Hoxotope S/N mentioned earlier. The fit intercept of 0.96 ppmv is significant and provides more evidence of the need for a systematic evaluation of the agreement between water vapor measurements. AVE-WIIF data alone are insufficient to conclusively identify the source of the disagreement, but a contamination offset may contribute part of the

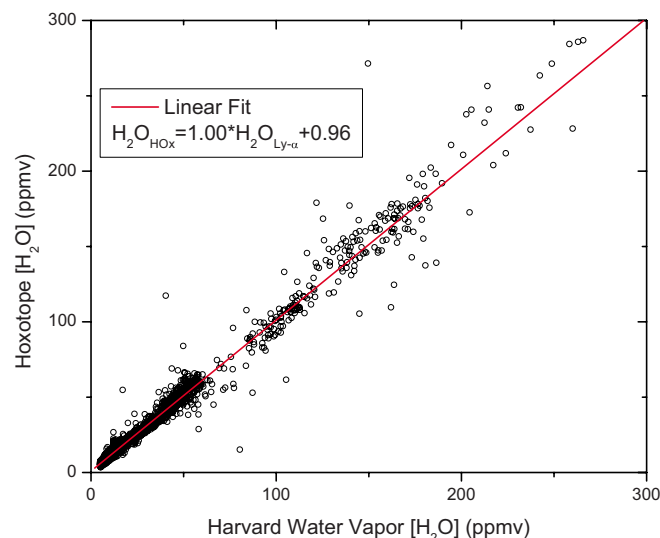


FIG. 11. (Color online) Hoxotope  $\text{H}_2\text{O}$  is plotted vs HWV  $\text{H}_2\text{O}$  for all three flights of AVE-WIIF. The symbols are the observed  $\text{H}_2\text{O}$  data and the data are fit to a line with a slope of 1.00 and an  $R^2$  value of 0.98.

offset. The data for the two instruments are shown as a time series in Fig. 12, top panel. Hoxotope tracks well with the open-throat HWV instrument, covering large changes in  $[\text{H}_2\text{O}]$ . When the fractional difference between the two instruments is plotted as a function of time (Fig. 12, bottom panel), with the exception of the ascent for every flight and parts of the July 5th flight, the fractional difference stays within the 95% confidence ( $2\sigma$ ) envelope for the Hoxotope measurement. The uncertainty shown is a combination of precision and the 5% accuracy—the difference between the measurements is therefore dominated by Hoxotope precision. The uncertainty is reported as a combination of accuracy and precision to properly represent the total data confidence level and highlight measurement artifacts.

Both time series reveal a water contamination experienced by Hoxotope early in each flight. ICOS, also a pallet instrument, recorded a similar contamination each flight. The contamination appears only on ascent and so is not a result of continuous outgassing; Hoxotope  $\text{H}_2\text{O}$  coincides with HWV  $\text{H}_2\text{O}$  upon exiting high water regions later in the flights. For example, there is no measurable difference between the two instruments on July 3rd after exiting 350 ppmv  $\text{H}_2\text{O}$  into 25 ppmv  $\text{H}_2\text{O}$  (at 18.5 h, July 3rd in Fig. 11, top panel). This high water feature, as well as all others later in each flight, stands in stark contrast to the measurement difference between the instruments on ascent.

Prior to flight, Hoxotope purges with  $\text{N}_2$  and ICOS seals off the instrument at its pinch valve. Both instruments are sealed off on ascent through the boundary layer, and both have flush times considerably shorter than the length of the contamination on ascent. Considering the incongruent time scales involved, the localization of the contamination to the ascent, and the nearly identical contamination of ICOS, the evidence is consistent with a source external to the instrument, thus implicating water coming from the airplane fuselage. The contamination, then, is likely an issue of instrument placement and inlet distance from the fuselage. The inlet has since been redesigned to extend further out of the

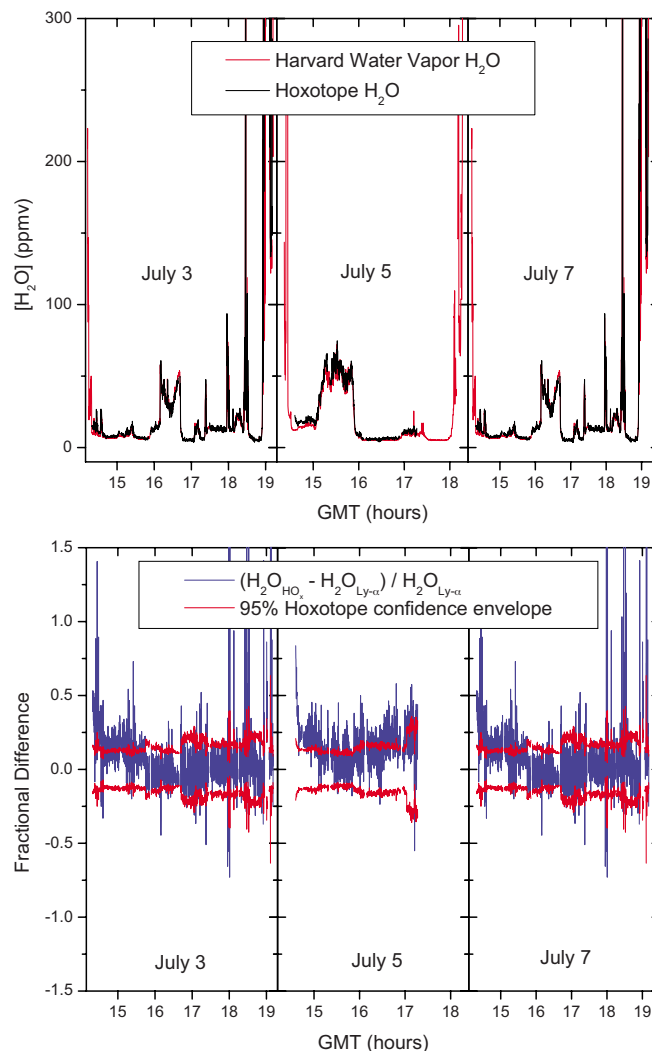


FIG. 12. (Color online) Top panel: HWV and Hoxotope  $[\text{H}_2\text{O}]$  data for the 2005 AVE-WIIF is shown as a time series for flights on July 3rd, 5th, and 7th. Bottom panel: fractional difference between HWV and Hoxotope is shown as a function of time. Also shown is the  $2\sigma$  uncertainty of Hoxotope determined from the calibration uncertainty (5%) and precision uncertainty.

fuselage boundary layer. On July 5th, Hoxotope  $\text{H}_2\text{O}$  deviated from HWV  $\text{H}_2\text{O}$  for reasons not related to sampling: Hoxotope laser performance issues were sufficiently severe that the laboratory calibration did not hold and a proper correction with  $\text{N}_2$  Raman was not possible.

The measurements of HDO are compared in Figs. 13 and 14. Hoxotope HDO and ICOS HDO agree over most of the three AVE-WIIF flights, though the agreement is not as close as between Hoxotope  $\text{H}_2\text{O}$  and HWV  $\text{H}_2\text{O}$ . The ICOS HDO data were filtered to remove all data for pressures below 100 mbar (10 kPa) in an effort to eliminate parts of the flights where ICOS instrumental artifacts were clearly detrimental to data quality; the data filtering removed the most serious of the disagreement between ICOS HDO and Hoxotope HDO. Figure 13 displays the regression of the two HDO measurements, with the fit including data with  $[\text{H}_2\text{O}] \leq 200$  ppmv. The agreement between the two new instruments, over almost three orders of magnitude in  $[\text{HDO}]$ , is notable: the measurements use fundamentally different techniques, the instruments were calibrated independently,

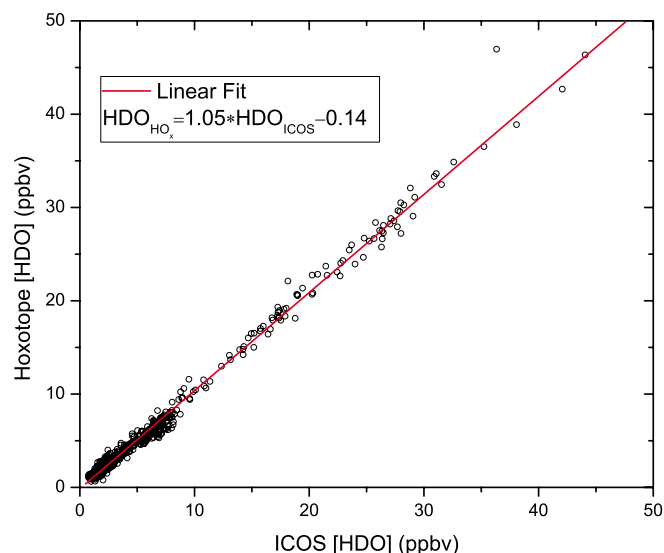


FIG. 13. (Color online) Symbols are the observed HDO from Hoxotope and ICOS, fit to a line with a slope of 1.05 and an  $R^2$  value of 0.99.

and the data were submitted blindly. The 5% difference in the calibration of the instruments is well within their stated accuracy. The top panel of Fig. 14 shows [HDO] measured by the two instruments, and the bottom panel shows the fractional difference between the two measurements in a time series. At times during the flights on July 3rd and 5th, poor instrument performance necessitated withholding data, resulting in the gaps seen in the time series. The causes were low laser power for Hoxotope and poor optical alignment for ICOS. On July 7th, no critical problems were encountered; that flight provides the longest data set for comparing the two instruments. The fractional difference shows that on average ICOS measures higher than Hoxotope, but the scatter is generally within the combined uncertainty of the two instruments.

## DISCUSSION

The requirements for an *in situ* water isotope instrument are demanding; failure to meet any one of several requirements would severely inhibit the ability of the measurement to provide a useful atmospheric tracer. A scientifically useful measurement must be accurate, with no instrument artifacts, and exhibit a precision and short sampling time constant sufficient to resolve atmospheric structure. The data from AVE-WIIF demonstrate the successful implementation of Hoxotope as an *in situ* water isotope instrument.

Regressions between Hoxotope and HWV for  $H_2O$  and Hoxotope and ICOS for HDO show that the instrument is well calibrated and confirms the general accuracy of Hoxotope  $H_2O$  and HDO. AVE-WIIF data also show that Hoxotope is free from the regular appearance of intractable instrument artifacts, with the exception of a sampling error on ascent; the contamination error will be solved by improving the sampling inlet. Instrument performance did affect accuracy on the July 5th flight, when poor optical alignment invalidated the instrument calibration and caused a 5%–10% bias in the data. Low laser power kept the instrument from achieving the precision it has demonstrated in lab

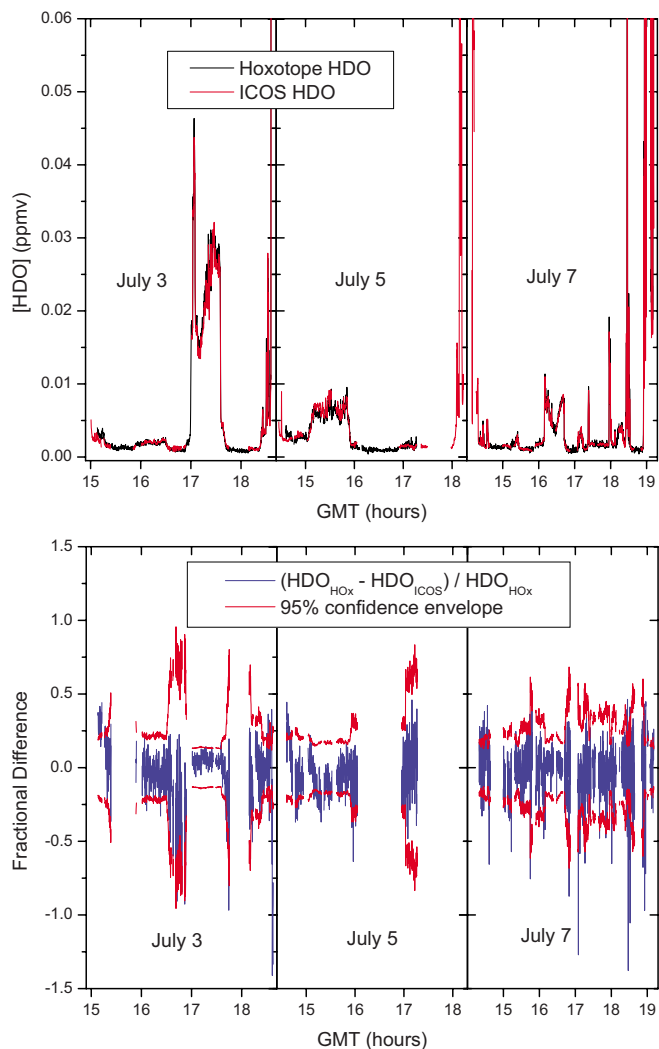


FIG. 14. (Color online) Top panel: ICOS and Hoxotope HDO data for July 3rd, 5th, and 7th during AVE-WIIF. Bottom panel: the fractional difference between ICOS and Hoxotope is shown as a time series for the three flights. The combined  $2\sigma$  precision for the instruments is included as an uncertainty envelope.

( $S/N > 20$  for 1 ppbv HDO over 10 s). The precision obtained during AVE-WIIF ( $S/N = 7$  for HDO in the stratosphere), however, was still sufficient to provide a data set with scientifically interesting features (i.e., Hanisco *et al.*<sup>24</sup>). So while normal instrument operation provides a level of precision ideal for resolving atmospheric structure, even sub-par performance is still of a high enough level that it produces quality data.

The uniquely short sampling time constant of Hoxotope was also demonstrated in AVE-WIIF: Hoxotope  $H_2O$  coincided with the ram air-fed HWV  $H_2O$ , excluding the ascent. The quick time response is due to the radical production technique of detecting water—it reduces the propensity of the instrument to retain water, beyond what is possible with a molecular detection technique. Because of its rapid response to changing water concentrations, Hoxotope is uniquely suited to future configuration as a total (vapor+condensed phase) water isotopes instrument. In summary, Hoxotope provides a  $1\sigma$  accuracy of  $\pm 5\%$  for both  $H_2O$  and HDO. The corresponding accuracy of the ratio expressed as  $\delta D$  is better

than 50‰ for the range of  $\delta D$  observed in the UT and LS ( $\delta D < -200‰$ ). During AVE-WIIF, the instrument achieved  $S/N=7$  for 1 ppbv HDO and  $S/N=12$  for 5 ppmv  $H_2O$  in a 10 s time interval, lower than its typical laboratory performance of  $S/N > 20$  for 1 ppbv HDO and  $S/N > 30$  for 5 ppmv  $H_2O$ . For these typical stratospheric values the signal to noise of the ratio was 7 during AVE-WIIF compared to  $S/N > 17$  in the laboratory.

There are many improvements possible for Hoxotope, largely because its development from the existing  $HO_x$  means much of the instrument is older and not necessarily optimal for its new role as Hoxotope. This development reality is worth bearing in mind when considering the construction of Hoxotope—some of the design is the way it is because of measurement need, and some of it is not optimized to the new measurement because it was not vital to instrument function. With a thorough redesign, it would be possible to lighten the instrument by 50 kg or more as well as reduce its volume and improve its operational stability.

Even with its current configuration, Hoxotope is capable of producing accurate, artifact-free data and has proven its value as a complimentary technique to properly evaluate and validate ICOS as a viable  $H_2O$  and HDO measurement. Such a thorough intercomparison is critical to the successful development and addition of a new measurement to an atmospheric payload. Because of the care taken in the technique development, calibration, and laboratory evaluation of Hoxotope, combined with the flight intercomparison between Hoxotope, ICOS, and HWV, a credible *in situ*  $\delta D$  data set in the UT/LS with geographic and seasonal variation is finally possible.

## SUMMARY

We have built and successfully flown an instrument capable of making scientifically useful measurements of  $\delta D$  in the UT and LS by employing a photolysis-LIF technique to measure  $H_2O$  and HDO concentrations. Hoxotope has the requisite sensitivity, accuracy, time response, and lack of systematic biases necessary to make a credible  $\delta D$  measurement and has demonstrated those same attributes both in the laboratory and in flight aboard the NASA WB-57. The instrument was subjected to an extensive, carefully designed laboratory calibration both before and after the AVE-WIIF campaign. Data from the AVE-WIIF series allowed for intercomparison of Hoxotope water with the established HWV instrument. The data clearly show a close agreement between the calibrations of the two instruments and they demonstrate the rapid time response of Hoxotope, with the exclusion of the beginning of each flight where aircraft outgassing was apparent—an issue easily rectified by instrument relocation and inlet extension. AVE-WIIF also allowed for intercomparison between Hoxotope HDO and ICOS HDO. The two techniques agree within stated uncertainty when instrument performance for both was sufficient to suggest confidence in the data. The successful intercomparison between Hoxotope  $H_2O$  and HWV  $H_2O$ , and between Hoxotope HDO and ICOS HDO, validated Hoxotope as a credible source of  $\delta D$  data in the UT and LS.

## ACKNOWLEDGMENTS

We thank the pilots and crew of the NASA WB-57, the logistical support of NASA Ames and NASA Johnson, and the engineering staff of the Harvard group for making the measurements possible. This work was supported by the NASA Upper Atmospheric Research Program.

- <sup>1</sup>D. Kley, J. M. Russell III, and C. Phillips, SPARC Report No. 2, WCRP-113, WMO/TD-1043 WMO/ICSU/IOC, CNRS, Verriere le Bruisson, 2000.
- <sup>2</sup>D. B. Kirk-Davidoff, E. J. Hints, J. G. Anderson, and D. W. Keith, *Nature (London)* **402**, 399 (1999).
- <sup>3</sup>D. T. Shindell, *Geophys. Res. Lett.* **28**, 1551 (2001).
- <sup>4</sup>P. M. D. Forster and K. P. Shine, *Geophys. Res. Lett.* **29**, 1086 (2002).
- <sup>5</sup>B. J. Soden, D. L. Jackson, V. Ramaswamy, M. D. Schwarzkopf, and X. L. Huang, *Science* **310**, 841 (2005).
- <sup>6</sup>K. H. Rosenlof, *Science* **302**, 1691 (2003).
- <sup>7</sup>J. R. Holton and A. Gettelman, *Geophys. Res. Lett.* **28**, 2799 (2001).
- <sup>8</sup>A. E. Dessler and S. C. Sherwood, *J. Geophys. Res., [Atmos.]* **109**, D23301 (2004).
- <sup>9</sup>H. Su, W. G. Read, J. H. Jiang, J. W. Waters, D. L. Wu, and E. J. Fetzer, *Geophys. Res. Lett.* **33**, L05709 (2006).
- <sup>10</sup>E. Moyer, F. Irion, Y. Yung, and M. Gunson, *Geophys. Res. Lett.* **23**, 2385 (1996).
- <sup>11</sup>D. Keith, *J. Geophys. Res., [Atmos.]* **105**, 15167 (2000).
- <sup>12</sup>H. Craig, *Science* **133**, 1833 (1961).
- <sup>13</sup>W. Dansgaard, *Tellus* **16**, 436 (1964).
- <sup>14</sup>D. Ehhalt, F. Rohrer, and A. Fried, *J. Geophys. Res., [Atmos.]* **110**, D13301 (2005).
- <sup>15</sup>D. G. Johnson, K. W. Jucks, W. A. Traub, and K. V. Chance, *J. Geophys. Res., [Atmos.]* **106**, 12211 (2001).
- <sup>16</sup>M. McCarthy, K. Boering, T. Rahn, J. Eiler, A. Rice, D. Tyler, S. Schauffler, E. Atlas, and D. Johnson, *J. Geophys. Res., [Atmos.]* **109**, D07304 (2004).
- <sup>17</sup>Z. Kuang, G. Toon, P. Wennberg, and Y. Yung, *Geophys. Res. Lett.* **30**, 1372 (2003).
- <sup>18</sup>C. R. Webster and A. J. Heymsfield, *Science* **302**, 1742 (2003).
- <sup>19</sup>D. G. Johnson, K. W. Jucks, W. A. Traub, and K. V. Chance, *J. Geophys. Res., [Atmos.]* **106**, 12219 (2001).
- <sup>20</sup>A. Dessler and S. Sherwood, *Atmos. Chem. Phys.* **3**, 2173 (2003).
- <sup>21</sup>A. Gettelman and C. R. Webster, *J. Geophys. Res., [Atmos.]* **110**, D17301 (2005).
- <sup>22</sup>R. Fu, Y. L. Hu, J. S. Wright, J. H. Jiang, R. E. Dickinson, M. X. Chen, M. Filipiak, W. G. Read, J. W. Waters, and D. L. Wu, *Proc. Natl. Acad. Sci. U.S.A.* **103**, 5664 (2006).
- <sup>23</sup>E. A. Ray, K. H. Rosenlof, E. C. Richard, P. K. Hudson, D. J. Cziczo, M. Loewenstein, H. J. Jost, J. Lopez, B. Ridley, A. Weinheimer, D. Montzka, D. Knapp, S. C. Wofsy, B. C. Daube, C. Gerbig, I. Xueref, and R. L. Herman, *J. Geophys. Res., [Atmos.]* **109**, D18304 (2004).
- <sup>24</sup>T. F. Hanisco, E. J. Moyer, E. M. Weinstock, J. M. St Clair, D. S. Sayres, J. B. Smith, R. Lockwood, J. G. Anderson, A. E. Dessler, F. N. Keutsch, J. R. Spackman, W. G. Read, and T. P. Bui, *Geophys. Res. Lett.* **34**, L04814 (2007).
- <sup>25</sup>P. O. Wennberg, R. C. Cohen, N. L. Hazen, L. B. Lapson, N. T. Allen, T. F. Hanisco, J. F. Oliver, N. W. Lanham, J. N. Demusz, and J. G. Anderson, *Rev. Sci. Instrum.* **65**, 1858 (1994).
- <sup>26</sup>D. Kley and E. J. Stone, *Rev. Sci. Instrum.* **49**, 691 (1978).
- <sup>27</sup>S. P. Sander, B. J. Finlayson-Pitts, R. R. Friedl, D. M. Golden, R. E. Huie, H. Keller-Rudek, C. E. Kolb, M. J. Kurylo, M. J. Molina, G. K. Moortgat, V. L. Orkin, A. R. Ravishankara, and P. H. Wine, *Chemical Kinetics and Photochemical Data for Use in Atmospheric Studies, Evaluation Number 15* (Jet Propulsion Laboratory, Pasadena, CA, 2006).
- <sup>28</sup>N. Shafer, S. Satyapal, and R. Bersohn, *J. Chem. Phys.* **90**, 6807 (1989).
- <sup>29</sup>J. Z. Zhang, D. G. Imre, and J. H. Frederick, *J. Phys. Chem.* **93**, 1840 (1989).
- <sup>30</sup>B. M. Cheng, E. P. Chew, C. P. Liu, M. Bahou, Y. P. Lee, Y. L. Yung, and M. F. Gerstell, *Geophys. Res. Lett.* **26**, 3657 (1999).
- <sup>31</sup>C. Y. Chung, E. P. Chew, B. M. Cheng, M. Bahou, and Y. P. Lee, *Nucl. Instrum. Methods Phys. Res. A* **467**, 1572 (2001).

- <sup>32</sup>K. Watanabe, E. C. Y. Inn, and M. Zelikoff, *J. Chem. Phys.* **21**, 1026 (1953).
- <sup>33</sup>G. H. Dieke and H. M. Crosswhite, *J. Quant. Spectrosc. Radiat. Transf.* **2**, 97 (1962).
- <sup>34</sup>G. Stark, J. W. Brault, and M. C. Abrams, *J. Opt. Soc. Am. B* **11**, 3 (1994).
- <sup>35</sup>J. R. Gillis, A. Goldman, G. Stark, and C. P. Rinsland, *J. Quant. Spectrosc. Radiat. Transf.* **68**, 225 (2001).
- <sup>36</sup>G. L. Vaghjiani and A. R. Ravishankara, *J. Chem. Phys.* **87**, 7050 (1987).
- <sup>37</sup>K. L. Steffens and D. R. Crosley, *J. Chem. Phys.* **112**, 9427 (2000).
- <sup>38</sup>E. M. Weinstock, E. J. Hintsa, A. E. Dessler, J. F. Oliver, N. L. Hazen, J. N. Demusz, N. T. Allen, L. B. Lapson, and J. G. Anderson, *Rev. Sci. Instrum.* **65**, 3544 (1994).
- <sup>39</sup>D. Sayres, E. J. Moyer, T. F. Hanisco, J. M. St. Clair, F. N. Keutch, J. N. Demusz, M. Rivero, N. T. Allen, L. B. Lapson, J. B. Paul *et al.*, available as part of D. S. Sayres' thesis at <http://www.arp.harvard.edu/atmobs/sciobj/instrument/IcosInstrumentPaper.pdf>.
- <sup>40</sup>R. K. Lengel and D. R. Crosley, *J. Chem. Phys.* **68**, 5309 (1978).
- <sup>41</sup>K. R. German, *J. Chem. Phys.* **63**, 5252 (1975).
- <sup>42</sup>K. R. German, *J. Chem. Phys.* **64**, 4065 (1976).
- <sup>43</sup>P. M. Selzer and C. C. Wang, *J. Chem. Phys.* **71**, 3786 (1979).
- <sup>44</sup>R. A. Copeland and D. R. Crosley, *J. Chem. Phys.* **84**, 3099 (1986).
- <sup>45</sup>R. A. Copeland, M. L. Wise, and D. R. Crosley, *J. Phys. Chem.* **92**, 5710 (1988).
- <sup>46</sup>J. Burris, J. J. Butler, T. J. McGee, and W. S. Heaps, *Chem. Phys.* **124**, 251 (1988).
- <sup>47</sup>I. S. McDermid and J. B. Laudenslager, *J. Chem. Phys.* **76**, 1824 (1982).